The astrochemical factory: A solid base for interstellar reactions

Ligterink, N.F.W.

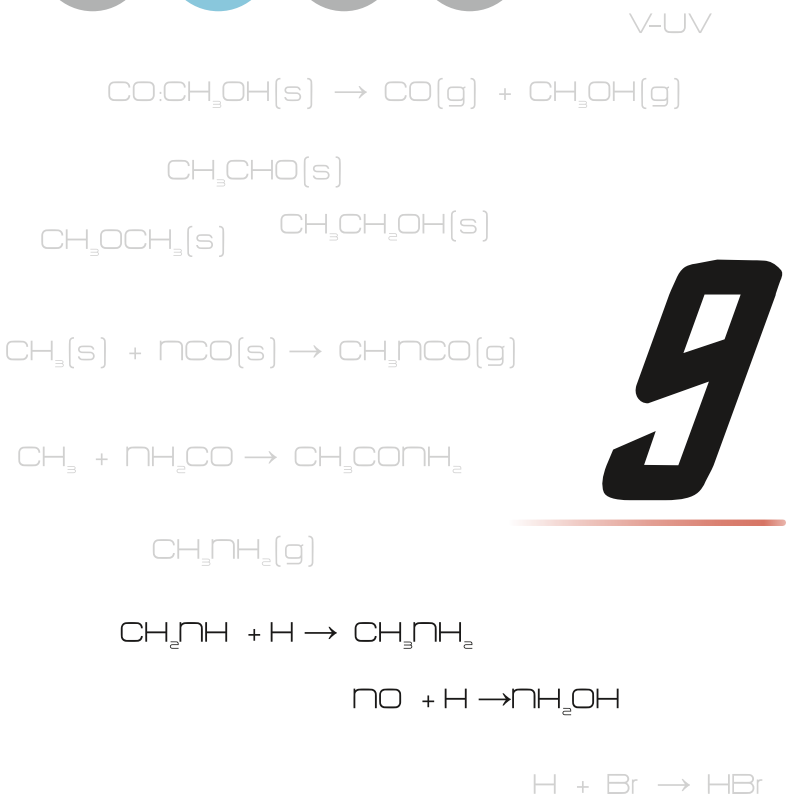

9

Small -NH_2 and NO molecules towards IRAS 16293–2422B

N.F.W. Ligterink, H. Calcutt, A. Coutens, T.L. Bourke, M.N. Drozdovskaya, L.E. Kristensen, H.S.P. Müller, S.F. Wampfler, M.H.D. van der Wiel, E.F. van Dishoeck & J.K. Jørgensen

Ligterink et al. 2017, *The ALMA-PILS survey: Stringent limits on small amines and nitrogen-oxides towards IRAS 16293–2422B*, subm. to A&A

9.1. Introduction

The small molecules methylamine (CH_3NH_2) and hydroxylamine (NH_2OH) with an amine (-NH_2) functional group have both been suggested as precursors to the formation of amino acids (Blagojevic et al. 2003; Snow et al. 2007; Holtom et al. 2005; Bossa et al. 2009; Barrientos et al. 2012; Garrod 2013). Reactions involving these molecules might explain the presence of the simplest amino acid glycine in comets (Elsila et al. 2009; Altwegg et al. 2016). Despite their importance, both CH_3NH_2 and NH_2OH have turned out to be quite elusive molecules in the interstellar medium. CH_3NH_2 has exclusively been detected towards Sgr B2 and tentatively towards Orion KL (e.g., Kaifu et al. 1974; Pagani et al. 2017). Upper limit abundances of CH_3NH_2 towards other high-mass sources are generally found to be consistent to values determined towards Sgr B2 (Ligterink et al. 2015). In the Solar System CH_3NH_2 has been detected in comets 81P/Wild 2 and 67P/Churyumov-Gerasimenko (Elsila et al. 2009; Goesmann et al. 2015; Altwegg et al. 2017). NH_2OH has not been detected thus far, down to upper limit abundances of $\sim 10^{-11}$ with respect to H_2 (Pulliam et al. 2012; McGuire et al. 2015).

The lack of detection of these two molecules not only constrains amino acid formation, but also contrasts with model predictions. Garrod et al. (2008) predicted efficient CH_3NH_2 formation from the radical addition reaction CH_3 + NH_2, whereas NH_2OH is formed from NH + OH addition followed by hydrogenation and NH_2 + OH reactions on ice surfaces. Abundances of CH_3NH_2 and NH_2OH are predicted to be of the order of 10^{-6}–10^{-7}, depending on the model. It is generally found that these models overproduce both molecules (Pulliam et al. 2012; Ligterink et al. 2015). Other formation or destruction mechanisms may need to be considered. Several laboratory experiments have investigated the formation of NH_2OH and CH_3NH_2. Zheng & Kaiser (2010) show the formation of NH_2OH from electron irradiated H_2O:NH_3 ice mixtures, while He et al. (2015) produce the molecule by oxidation of NH_3 ice. Alternatively, NH_2OH is seen to efficiently form from the solid-state hydrogenation of nitric oxide (NO, Congiu et al. 2012; Fedoseev et al. 2012). In this scenario, NO is accreted from the gas-phase onto dust grains during cloud collapse (Visser et al. 2011). Nitrous oxide (N_2O) is found as a by-product of NO hydrogenation reactions. NO has been observed in a variety of sources (e.g., Liszt & Turner 1978; Yıldız et al. 2013). It is thought to mainly form via the N + OH $\rightarrow$ NO + H neutral-neutral reaction in the gas-phase. Observations suggest that N_2O is related to NO (Ziurys et al. 1994; Halfen et al. 2001).

CH_3NH_2 formation has been demonstrated in electron irradiated CH_4:NH_3 ice mixtures (Kim & Kaiser 2011; Förstel et al. 2017), with the main formation pathways suggested to proceed through CH_3 + NH_2 radical reactions. Theule et al. (2011) investigated hydrogenation of solid hydrogen cyanide (HCN) and methanimine (CH_2NH), both of which lead to CH_3NH_2 formation. CH_2NH is hypothesized to have a larger reaction probability than HCN and reaction pathways to CH_3NH_2 may be completely different for reactions starting from either HCN or CH_2NH. In contrast with CH_3NH_2, its potential precursor CH_2NH has been observed in numerous sources (Dickens et al. 1997; Nummelin et al. 2000; Belloche et al. 2013; Suzuki et al. 2016). Halfen et al. (2013) investigated

the relationship between this molecule and CH_3NH_2 in Sgr B2 and concluded that the two species have different formation routes, due to found differences in rotational temperature and distribution. Interestingly, CH_2NH has also been implied as a precursor to amino acid formation (e.g., Woon 2002; Danger et al. 2011).

Searches for CH_3NH_2 and NH_2OH have so far mainly focused on high-mass sources. Detections or upper limits of these two molecules and their potential precursors towards a low-mass source would therefore expand our understanding of amine-containing molecules and their formation in the ISM. The low-mass solar-type protostellar binary IRAS 16293–2422 (hereafter IRAS 16293) is an ideal source for such a study. Its physics and chemistry are well studied and it is abundant in complex organic molecules (Jørgensen et al. 2016). Abundance ratios will therefore constrain the chemistry of -NH_2 molecules as has been done for other nitrogen-bearing species (Coutens et al. 2016; Ligterink et al. 2017). In this letter we present the first detection of CH_2NH towards a low-mass source, as well as detections of NO and N_2O. The abundances of NH_2OH and CH_3NH_2 are constrained by upper limits from non-detections.

9.2. Observations and data analysis

The observations were taken as part of the Protostellar Interferometric Line Survey (PILS), an unbiased spectral survey using the Atacama Large Millimeter Array (ALMA, Jørgensen et al. 2016). The survey covers a spectral range of 329.147 to 362.896 GHz in Band 7, obtained with the 12 m array and the Atacama Compact Array (ACA). The combined data set analysed in this letter was produced with a circular restoring beam of $0\farcs5$. The largest filtered scale is $13''$. A spectral resolution of 0.2 km s^{-1} and an RMS of about 7–10 mJy beam^{-1} channel^{-1}, i.e., approximately 4–5 mJy beam^{-1} km s^{-1} is obtained. The dataset has a calibration uncertainty of 5-10%.

The spectral analysis presented below is performed towards source B in IRAS 16293 at a position offset by one beam diameter ($0\farcs5$) from the continuum peak position in the south west direction (α_{J2000}=16^{h}32^{m}22$\fs$58, δ_{J2000}=$-$24°28′32.8″). This position is used for most other PILS molecular identifications and abundance analyses. Lines are particularly narrow towards this position, only 1 km s^{-1}, limiting line confusion.

The spectra are analysed with the CASSIS software[1] and linelists from the Jet Propulsion Laboratory (JPL[2]) catalog for molecular spectroscopy (Pickett et al. 1998) and Cologne Database for Molecular Spectroscopy (CDMS, Müller et al. 2001, 2005). The detected transitions are fitted with synthetic spectra to derive column densities, excitation temperatures, linewidths and peak velocities assuming Local Thermodynamic Equilibrium (LTE) and a source size of $0\farcs5$ based on emission maps of the source.

Due to the strong continuum component towards IRAS 16293B, the continuum is included in the spectral model as a background temperature. The continuum is dominated by the high column density dust in the disk while the

[1] http://cassis.irap.omp.eu/
[2] http://spec.jpl.nasa.gov

Table 9.1: Column densities for the species investigated in this work.

Molecule	Formula	$N_{tot}^{\dagger}$ (cm^{-2}) (cm^{-2})	T_{ex} (K) (K)	FWHM ($km\,s^{-1}$) ($km\,s^{-1}$)	V_{peak} ($km\,s^{-1}$) ($km\,s^{-1}$)
Nitric oxide	NO	$2.0\ (0.5)\times10^{16}$	100^{+50}_{-60}	1.0	2.5
Nitrous oxide	N_2O	$5.0\ (1.0)\times10^{16}$	100^{+150}_{-20}	1.0	2.5
Hydroxylamine	NH_2OH	$\leq3.7\times10^{14}$	100	1.0	2.7
Methanimine	CH_2NH	$8.0\ (2.0)\times10^{14}$	100^{+20}_{-30}	1.0	2.7
Methylamine	CH_3NH_2	$\leq5.3\times10^{14}$	100	1.0	2.7

Notes. All models assume LTE, an excitation temperature of 100 K, a FWHM of $1\,km\,s^{-1}$ and a source size of 0.″5. †Upper limits are 3σ.

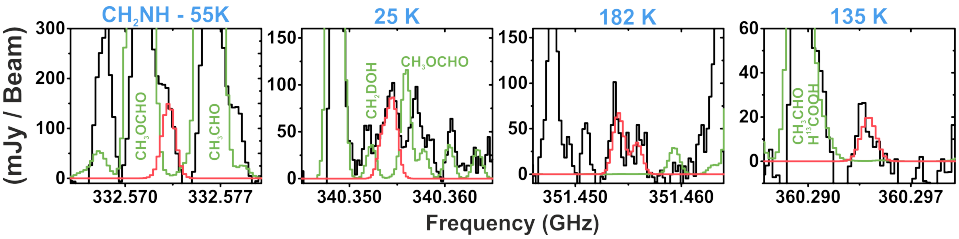

Figure 9.1: All detected transitions of CH_2NH in the PILS spectrum (black), with the best fit at T_{ex} = 100 K (red) and template of other detected species in PILS overplotted (green). The upper state energy of each transition is indicated in blue.

lines arise from the infalling gas in the envelope, and therefore the dust and gas are not fully coupled at the offset position analysed in this work. The correction factor is 1.15 at 100 K.

For the non-detected species the formalism in Ligterink et al. (2015) is used to derive upper limit column densities based on the 3σ upper limit line intensities of the strongest transitions in line-free ranges of the PILS data. The 1σ limit is given by $1.1\times\Delta V\times$RMS, where ΔV is the linewidth in source B ($1\,km\,s^{-1}$) and 1.1 is a factor to account for a 10% calibration uncertainty. Corrections for beam dilution and background dust temperature are applied as well.

9.3. Results

Spectral lines of CH_2NH, NO and N_2O are identified towards source B, while those of CH_3NH_2 and NH_2OH are not. An overview of the detected transitions is presented in Table 9.4 in Appendix A. Figures 9.1, 9.2 and 9.3 show the detected transitions of CH_2NH, NO and N_2O, respectively, towards source B, with synthetic spectra overplotted. A synthetic spectrum of other species identified in the framework of PILS is also plotted to show which lines are blended.

CH_2NH is detected for the first time towards a low-mass protostellar source. A total of 18 hyperfine lines in four different spectral features are detected. The first feature shows up at 332.575 GHz and is blended with a neighbouring CH_3OCHO line. At 340.354 GHz five hyperfine lines form a distinct feature

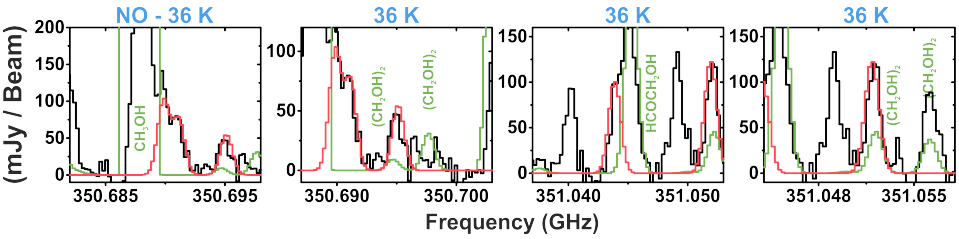

Figure 9.2: All detected transitions of NO in the PILS spectrum (black), with the best fit at T_{ex} = 100 K (red) and template of other detected species in PILS overplotted (green). The upper state energy of each transition is indicated in blue.

that is unblended with any other molecule. Around 351.455 GHz a distinct double peak feature is found. Finally, at 360.294 GHz the last feature is seen, that seems to be blended with another, unidentified feature. ALMA observations in bands 4, 6 and 9 towards IRAS 16293 were used to search for additional lines, but spectral features of CH_2NH fall outside the spectral windows of these observations. Publicly available data of the single dish TIMASSS survey towards IRAS 16293 were analysed for CH_2NH spectral features, but no lines were found.

Upper state energies (E_{up}) of the detected features range from 26 to 183 K, making it possible to constrain the excitation temperature. With a grid of models the emission of this species can be fitted with excitation temperatures ranging between 70–120 K and column densities of 6.0×10^{14} – 10.0×10^{14} cm^{-2}. Outside this temperature range synthetic spectra can not reproduce the observed spectrum, as can be seen in Fig. 9.5 in Appendix 9.5.2 for fits at T_{ex} = 50 and 150 K. In the best fits, no anti-coincidences are found between the synthetic and observed spectrum. At T_{ex} = 100 K the best fit column density is found to be 8.0×10^{14} cm^{-2}.

Five NO transitions, each with an upper state energy of 36 K, are detected. A number of NO lines at E_{up} = 209 K are in range of the data, but are not observed in the spectrum. The excitation temperature can therefore be constrained to be lower than 150 K, due to anti-coincidences of the E_{up} = 209 K lines in the synthetic spectrum at 150 K and higher, as can be seen in Fig. 9.6 in Appendix 9.5.2. At an excitation temperature of 100 K a best fit column density of 2.0×10^{16} cm^{-2} is found, but it can vary between 1.5×10^{16} – 2.5×10^{16} cm^{-2} for T_{ex} 40 – 150 K. The emission is best fitted with a velocity of V_{peak} = 2.5 km s^{-1}, slightly offset from the V_{LSR} = 2.7 km s^{-1} of source B. A similar offset is seen in some other species in the PILS dataset (see Jørgensen et al. in preparation for more details), however this offset only corresponds to 1 velocity channel in the data. We therefore can't interpret this difference at this time.

Three N_2O transitions fall in the frequency range of the PILS data, one v=0 line, E_{up} = 127 K and two v_2=1 lines, E_{up} = 973 K. In the observed spectrum a feature is found that fits the v=0 line at 351.667 GHz. Since no other known species were found to fit this spectral feature, a tentative detection of N_2O can be claimed. We have also searched additional datasets to try and find further lines to support this detection. We have searched band 4, 6 and 9 ALMA datasets towards IRAS 16293, as well as data from the single dish TIMASSS survey. We

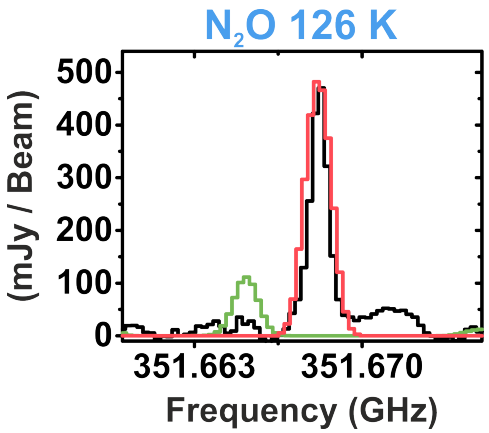

Figure 9.3: The tentatively identified transition of N_2O in the PILS spectrum (black), with the best fit at T_{ex} = 100 K (red) and template of other detected species in PILS overplotted (green). The upper state energy of each transition is indicated in blue.

are however unable to detect more lines as those that fall in the frequency range of the data are too weak to be identified. Similar to NO, V_{peak} = 2.5 km s^{-1} for this line. Lines of the ^{15}N and ^{18}O isotopologues of N_2O were searched for, but not detected to levels above the standard $^{15}N/^{14}N$ and $^{18}O/^{16}O$ ISM ratios. Based on the non-detection of the v_2=1 lines, the excitation temperature can be determined to be lower than 250 K. At T_{ex} = 100 K a column density of 5.0×10^{16} cm^{-2} for N_2O is derived, with an uncertainty of $\pm1.0\times10^{16}$ cm^{-2} over the entire possible temperature range.

Figure 9.4 shows the emission maps of the 332.572 GHz line of CH_2NH, the 351.052 GHz line of NO, and the 351.668 GHz line of N_2O towards source B. Emission is generally found to be compact and compares well with emission maps of other molecules towards source B, such as NH_2CHO (Coutens et al. 2016). Emission of N_2O is more extended than that of NO.

Transitions of both CH_3NH_2 and NH_2OH are not detected and therefore upper limit column densities are determined. For CH_3NH_2, the $6_1 \rightarrow 5_0$ transition at 357.440 GHz best constrains the upper limit column density. For a 3σ upper limit line intensity of 23 mJy km s^{-1} the upper limit column densities versus the rotational temperatures are plotted in Fig. 9.7 in Appendix C. At T_{ex} = 100 K the upper limit column density is $\leq5.3\times10^{14}$ cm^{-2}.

NH_2OH has three strong transitions at 352.522, 352.730 and 352.485 GHz for the $7_0 \rightarrow 6_0$, $7_1 \rightarrow 6_1$, $7_2 \rightarrow 6_2$ transitions, respectively. Slightly different RMS noise conditions apply around each of these transitions, resulting in a 3σ of 27, 21 and 27 mJy km s^{-1}, respectively. The upper limit column density versus rotational temperature plot is shown in Fig. 9.8. The transition at 352.522 GHz constrains the column density the most and the upper limit column density of NH_2OH is found to be $\leq3.7\times10^{14}$ cm^{-2} at T_{ex} = 100 K.

Table 9.1 lists the column densities at T_{ex} = 100 K for the five molecules under investigation in this work. The range of excitation temperatures that can fit the emission has been included in this Table and the resulting uncertainty in the

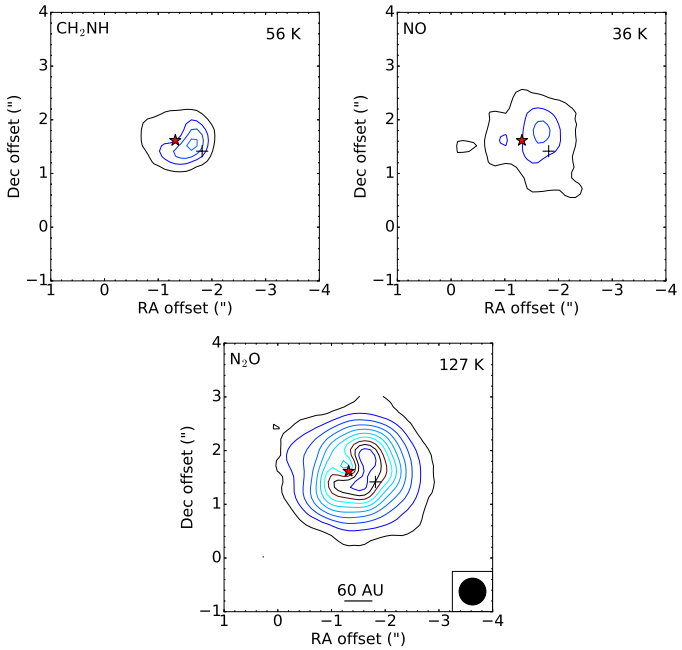

Figure 9.4: Integrated emission maps of the 332.572 GHz line of CH_2NH, the 351.052 GHz line of NO, and the 351.668 GHz line of N_2O. The emission is integrated between 2.2 and 3.2 km s^{-1}. The axes show the position offset from phase centre of the observations. Contour levels start at 20σ and increase in steps of 30σ. The red star marks the peak continuum position and the black cross marks the 1 beam offset position where the spectra are analysed.

column density is given in brackets. For both CH_3NH_2 and NH_2OH the typical uncertainty in column density for a reasonable range of excitation temperatures is a factor of $\sim$2.

Table 9.2: Comparison of methylamine abundance ratios.

Source	CH_3NH_2/CH_2NH	CH_3NH_2/NH_2CHO	CH_3NH_2/CH_3OH
IRAS 16293–2422B	$\leq$0.79	$\leq$0.053	$\leq 5.3\times10^{-5}$
Sgr B2[a]	$\sim$1	0.57	0.017
Sgr B2(M)[b]	31	3.2	0.017
Sgr B2(N)[b]	0.75	0.43	0.033
Sgr B2(N)[c]	5.5	–	–
Sgr B2(N)[d]	7.1	2.1	0.1
Hot core model[e]	–	1.1–1.7	0.034–0.13

Notes. [a]Turner (1991); [b]Belloche et al. (2013); [c]Halfen et al. (2013); [d]Neill et al. (2014); [e]Garrod et al. (2008), models F, M and S.

Table 9.3: Comparison of CH_2NH abundance ratios.

Source	CH_2NH/NH_2CHO	CH_2NH/CH_3OH	CH_2NH/H_2
IRAS 16293–2422B	0.08	8.0×10^{-5}	$<6.7\times10^{-11}$
Sgr B2[a]	$\sim$0.57	$\sim$0.017	–
Sgr B2(M)[b]	0.10	5.5×10^{-4}	–
Sgr B2(N)[b]	0.57	0.044	–
Sgr B2(N)[c]	–	–	3.0×10^{-10}
Sgr B2(N)[d]	0.30	0.014	8.8×10^{-9}
Orion KL[e]	–	1.9×10^{-3}	4.2×10^{-9}

Notes. [a]Turner (1991); [b]Belloche et al. (2013); [c]Halfen et al. (2013); [d]Neill et al. (2014); [e]Crockett et al. (2014b)

9.4. Astronomical implications

To put the results into context the abundance ratios with formamide, methyl cyanide, methanol and molecular hydrogen are compared with other sources. The column densities of these species towards the 1 beam offset position in source B are: $NH_2CHO = 1\times10^{16}$, $CH_3OH = 1\times10^{19}$ and $H_2 > 1.2\times10^{25}$ cm^{-2} (Coutens et al. 2016; Jørgensen et al. 2016). The H_2 lower limit column density is determined towards the continuum peak position of source B, but within the uncertainties of the observations is not expected to differ much for the one beam offset position being analysed in this chapter. Many papers with which our ratios are compared to make use of single dish data, whereas in this work we use interferometric data. It is important to stress that differences in abundance ratios do not necessarily reflect chemical differences, but could arise from the fact that single dish observations generally probe larger spatial scales and are more affected by beam dilution (see Jørgensen et al. 2016).

The NH_2OH upper limit abundance of $N(NH_2OH)/N(H_2) \leq 3.1\times10^{-11}$ found in this work is comparable to upper limit abundances found for high-mass sources by Pulliam et al. (2012), but significantly lower than the ice abundances of 7×10^{-9} $N(H+H_2)$ found with a dark cloud model in Fedoseev et al. (2012). However, this model does not take destruction and reaction pathways into account and could overpredict the NH_2OH abundance. The non-detection of NH_2OH in the gas-phase could be explained by efficient destruction of the molecule. Laboratory experiments show that thermal processing of NH_2OH:H_2O mixtures result in the conversion of NH_2OH into HNO, NH_3 and O_2 before the onset of desorption (Jonusas & Krim 2016). Also, UV processing of ice mixtures containing NH_2OH results in the efficient destruction of this molecule (Fedoseev et al. 2016). The low gas-phase abundance of NH_2OH limits its involvement in gas-phase production routes of amino acids.

The NO abundance in IRAS 16293B ($N(NO)/N(H_2) \leq 1.7\times10^{-9}$) is low compared to observational and modelling studies of dark clouds, where NO abundances of 10^{-8}–10^{-6} are found (e.g., McGonagle et al. 1990; Visser et al. 2011). Modelling shows that NO is readily lost in the ice by conversion to other species, mainly NH_2OH (Yıldız et al. 2013), and in the gas-phase by photodissociation reactions in the hot core (Visser et al. 2011) and thus could explain the depletion of NO in IRAS 16293B. The high N_2O abundance may indicate destruction of NO as well. It is found in laboratory ice experiments

as a side product of NO hydrogenation and UV irradiation (Congiu et al. 2012; Fedoseev et al. 2012, 2016) and suggested to form via the reaction NO + NH in warm gas (Halfen et al. 2001). The $N(N_2O)/N(NO)$ = 2.5 ratio may hint to a scenario where NO is depleted in the ice and gas surrounding IRAS 16293B, while N_2O is one of the products of NO.

Table 9.2 lists the abundance ratios of CH_3NH_2 in IRAS 16293B, Sgr B2 and hot core models of Garrod et al. (2008). Abundances differ by at least one to two orders of magnitude between IRAS 16293B and Sgr B2 and models. CH_2NH is also much less abundant in IRAS IRAS 16293B than Sgr B2 (Table 9.3). This can indicate that the formation of both species is less efficient in IRAS 16293B, perhaps due to different physical conditions of the sources. CH_3NH_2 was mass spectrometrically detected on the comet 67P/C-G (Goesmann et al. 2015). However, recent measurements with the ROSINA-DFMS instrument determined it to be present at lower abundance than initially thought (Altwegg et al. 2017). Since IRAS 16293B is assumed to resemble an early formation stage of our solar system, the low abundance of CH_3NH_2 and non-detection in IRAS 16293B suggest that CH_3NH_2 is not efficiently formed in these environments. The low abundance of CH_3NH_2 limits the relevance of amino acid formation routes involving this species. Conversely, the detection of CH_2NH makes amino acid formation routes involving this molecule a more relevant possibility.

Acknowledgement

This letter makes use of the following ALMA data: ADS/JAO.ALMA#2013.1.00278.S. ALMA is a partnership of ESO (representing its member states), NSF (USA) and NINS (Japan), together with NRC (Canada) and NSC and ASIAA (Taiwan), in cooperation with the Republic of Chile. The Joint ALMA Observatory is operated by ESO, AUI/NRAO and NAOJ. Astrochemistry in Leiden is supported by the European Union A-ERC grant 291141 CHEMPLAN, by the Netherlands Research School for Astronomy (NOVA) and by a Royal Netherlands Academy of Arts and Sciences (KNAW) professor prize. The group of J.K.J. acknowledges support from a Lundbeck Foundation Group Leader Fellowship, as well as the ERC under the European Union's Horizon 2020 research and innovation programme through ERC Consolidator Grant S4F (grant agreement No 646908). Research at the Centre for Star and Planet Formation is funded by the Danish National Research Foundation. A.C. postdoctoral grant is funded by the ERC Starting Grant 3DICE (grant agreement 336474).

9.5. Appendix

9.5.1. Spectroscopic data

Table 9.4 lists the transitions of NO, N_2O and CH_2NH detected towards IRAS 16293B (Pickett et al. 1979; Ting et al. 2014; Kirchhoff et al. 1973).

Table 9.4: Detected lines of NO, N_2O and CH_2NH.

Molecules	Transitions	Frequency (MHz)	E_{up} (K)	A_{ij} (s^{-1})	g_{up}	Blended	Database
NO	4 −1 7/2 9/2 – 3 1 5/2 7/2	350 689.49	36	5.42×10^{-6}	10	Y	JPL
NO	4 −1 7/2 7/2 – 3 1 5/2 5/2	350 690.76	36	4.97×10^{-6}	8	N	JPL
NO	4 −1 7/2 5/2 – 3 1 5/2 3/2	350 694.77	36	4.81×10^{-6}	6	N	JPL
NO	4 1 7/2 9/2 – 3 −1 5/2 7/2	351 043.52	36	5.43×10^{-6}	10	Y	JPL
NO	4 1 7/2 7/2 – 3 −1 5/2 5/2	351 051.46	36	4.99×10^{-6}	8	Y	JPL
NO	4 1 7/2 5/2 – 3 −1 5/2 3/2	351 051.70	36	4.83×10^{-6}	6	Y	JPL
N_2O	14 – 13	351 667.81	127	6.32×10^{-6}	29	N	JPL
CH_2NH	5 1 4 5 – 4 1 3 4	332 573.04	56	3.15×10^{-4}	11	Y	JPL
CH_2NH	5 1 4 6 – 4 1 3 5	332 573.07	56	3.28×10^{-4}	13	Y	JPL
CH_2NH	5 1 4 4 – 4 1 3 3	332 573.11	56	3.12×10^{-4}	9	Y	JPL
CH_2NH	3 1 3 3 – 2 0 2 3	340 353.05	26	3.44×10^{-5}	7	N	JPL
CH_2NH	3 1 3 3 – 2 0 2 2	340 353.37	26	2.75×10^{-4}	7	N	JPL
CH_2NH	3 1 3 4 – 2 0 2 3	340 354.31	26	3.09×10^{-4}	9	N	JPL
CH_2NH	3 1 3 2 – 2 0 2 1	340 354.58	26	2.60×10^{-4}	5	N	JPL
CH_2NH	3 1 3 2 – 2 0 2 2	340 355.08	26	4.81×10^{-5}	5	N	JPL
CH_2NH	10 1 9 9 – 10 0 10 9	351 453.85	183	3.61×10^{-4}	19	Y	JPL
CH_2NH	10 1 9 11 – 10 0 10 11	351 454.02	183	3.62×10^{-4}	23	Y	JPL
CH_2NH	10 1 9 10 – 10 0 10 9	351 454.43	183	3.30×10^{-6}	21	Y	JPL
CH_2NH	10 1 9 10 – 10 0 10 11	351 454.55	183	3.30×10^{-6}	21	Y	JPL
CH_2NH	10 1 9 11 – 10 0 10 11	351 454.02	183	3.62×10^{-4}	23	Y	JPL
CH_2NH	10 1 9 11 – 10 0 10 10	351 455.17	183	3.02×10^{-6}	23	Y	JPL
CH_2NH	10 1 9 10 – 10 0 10 10	351 455.70	183	3.58×10^{-4}	21	Y	JPL
CH_2NH	6 3 4 6 – 7 2 5 7	360 293.85	135	6.91×10^{-5}	13	Y	JPL
CH_2NH	6 3 4 7 – 7 2 5 8	360 294.05	135	6.93×10^{-5}	15	Y	JPL
CH_2NH	6 3 4 5 – 7 2 5 6	360 294.08	135	7.05×10^{-5}	11	Y	JPL

Notes. Quantum numbers are given as N′ K′ J′ F′ – N″ K″ J″ F″ for NO, J′ – J″ for N_2O and J′ K_a' K_c' F′ – J″ K_a'' K_c'' F″ for CH_2NH.

9.5.2. Additional fit spectra of CH_2NH and NO

Figure 9.5 shows CH_2NH synthetic spectra at T_{ex} 50 and 150 K. Best fit column densities of 7×10^{14} and 8×10^{14}, respectively, are found. However, clear discrepancies in the fits exist, which are especially visible for the transitions at 340.354 and 351.454 GHz.

Figure 9.6 shows the NO synthetic spectrum at T_{ex} 150 K and $N_{tot} = 2.3\times10^{16}$. The transitions at E_{up} = 36 K are well fitted, however, clear anti-coincidences start to arise at the transitions of E_{up} = 209 K, as can be seen for the transitions at 360.935 and 360.941 GHz. Excitation temperatures for NO are therefore constrained to $T_{ex} < 150$ K.

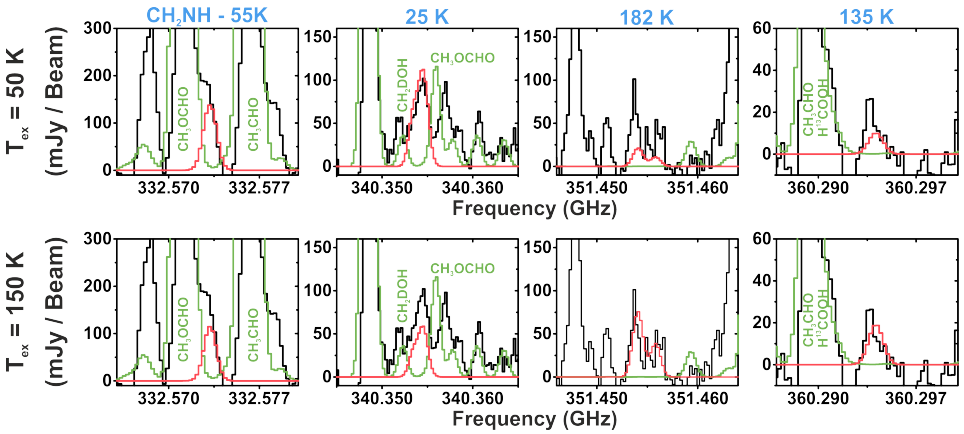

Figure 9.5: Fit models (red) of CH_2NH at T_{ex} = 50 K (top) and T_{ex} = 150 K (bottom) overplotted on the PILS data (black) and other detected species in PILS given in green. Upper state energies of the transitions are indicated in blue.

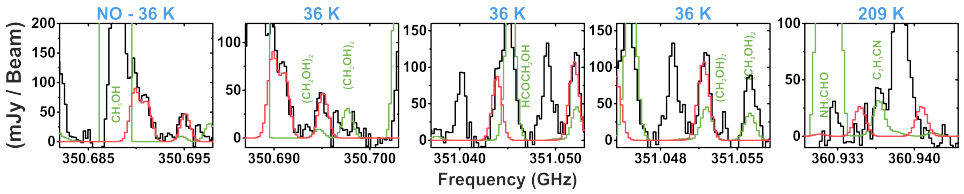

Figure 9.6: Fit models (red) of NO at T_{ex} = 150 K (bottom) overplotted on the PILS data (black) and other detected species in PILS given in green. Upper state energies of the transitions are indicated in blue.

9.5.3. Upper limit column densities of NH_2OH and CH_3NH_2

Upper limit column densities of NH_2OH and CH_3NH_2 have been determined for excitation temperatures between 10 and 300 K (Morino et al. 2000; Ilyushin et al. 2005). These are plotted in Figure 9.8 and 9.7. The upper limit column densities of NH_2OH are determined on the three transitions: $7_0 \rightarrow 6_0$, $7_1 \rightarrow 6_1$, $7_2 \rightarrow 6_2$ transitions at 352 522, 352 730 and 352 485 MHz, respectively. These transitions are modelled with a 3σ line intensity of 27, 21 and 27 mJy km s^{-1}, respectively. The upper limit column densities of CH_3NH_2 are determined on the $6_5 \rightarrow 5_0$ transition at 357 440 MHz for a 3σ line intensity of 23 mJy km s^{-1}.

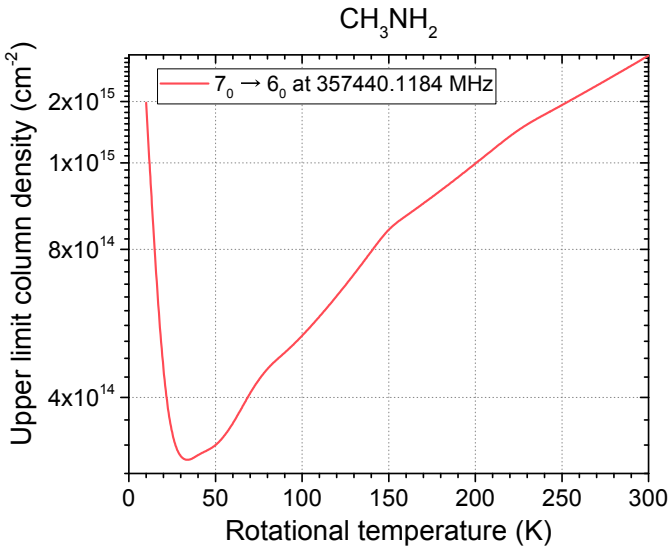

Figure 9.7: Upper limit column density for the strongest CH_3NH_2 transition. A 3σ value of 23 mJy km s^{-1} is used.

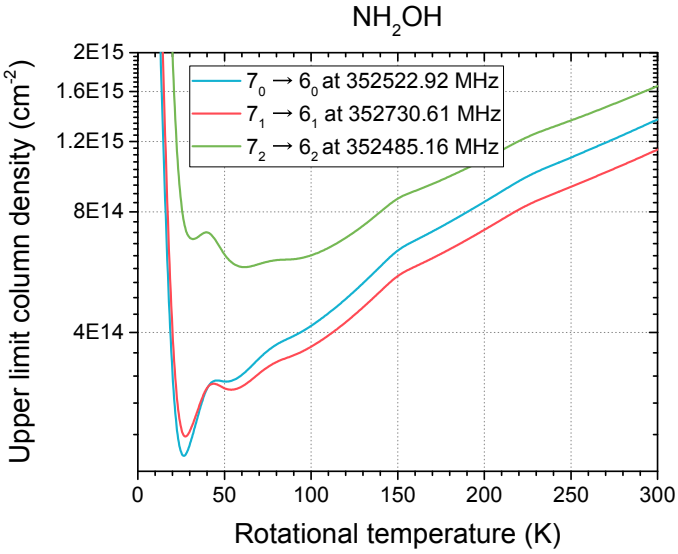

Figure 9.8: Upper limit column densities for the three strongest NH_2OH transitions. 3σ values of 27, 21 and 27 mJy km s^{-1} are used for the respective lines.